



HAL
open science

Feasibility demonstration of AO pre-compensation for GEO feeder links in a relevant environment

Aurélie Montmerle Bonnefois, Marie-Thérèse Velluet, Mahawa Cissé, Caroline Lim, Jean-Marc Conan, Cyril Petit, Jean-François Sauvage, Serge Meimon, Philippe Perrault, Joseph Montri, et al.

► To cite this version:

Aurélie Montmerle Bonnefois, Marie-Thérèse Velluet, Mahawa Cissé, Caroline Lim, Jean-Marc Conan, et al.. Feasibility demonstration of AO pre-compensation for GEO feeder links in a relevant environment. *Optics Express*, 2022, 30 (26), pp.47179. 10.1364/OE.470705 . hal-03898930

HAL Id: hal-03898930

<https://hal.science/hal-03898930>

Submitted on 20 Jan 2023

HAL is a multi-disciplinary open access archive for the deposit and dissemination of scientific research documents, whether they are published or not. The documents may come from teaching and research institutions in France or abroad, or from public or private research centers.

L'archive ouverte pluridisciplinaire **HAL**, est destinée au dépôt et à la diffusion de documents scientifiques de niveau recherche, publiés ou non, émanant des établissements d'enseignement et de recherche français ou étrangers, des laboratoires publics ou privés.



Feasibility demonstration of AO pre-compensation for GEO feeder links in a relevant environment

AURÉLIE MONTMERLE BONNEFOIS,^{*}  MARIE-THÉRÈSE VELLUET, MAHAWA CISSÉ, CAROLINE B. LIM, JEAN-MARC CONAN, CYRIL PETIT, JEAN-FRANÇOIS SAUVAGE, SERGE MEIMON,  PHILIPPE PERRAULT, JOSEPH MONTRI, AND NICOLAS VÉDRENNE

DOTA, ONERA, Université Paris Saclay, F-92322 Châtillon, France

^{*}aurelie.bonnefois@onera.fr

Abstract: Optical technologies are extremely competitive candidates to achieve very-high throughput links between ground and GEO satellites; however, their feasibility relies on the ability to mitigate channel impairments due to atmospheric turbulence. For that purpose, Adaptive Optics (AO) has already proved to be highly efficient on the downlink. However, for the uplink, anisoplanatism induced by point-ahead angle (PAA) compromises AO pre-compensation efficiency to an extent that depends on propagation conditions. The ability to properly assess the anisoplanatism impact in a wide variety of conditions is thus critical in designing the optical ground terminals. In this paper, we demonstrate the consistency of experimental coupled flux statistics with results coming from performance and end-to-end models, on an AO pre-compensated 13 km slant path in Tenerife. This validation is demonstrated in a wide variety of turbulence conditions, hence consolidating propagation channel models that are of critical importance for the reliability of future GEO feeder links. We then compare experimental results to theoretical on-sky performance, and discuss to what extent such slant path or horizontal path experiments can be representative of real GEO links.

© 2022 Optica Publishing Group under the terms of the [Optica Open Access Publishing Agreement](#)

1. Introduction

The current development of space data highways would significantly benefit from the possibility of exchanging Terabytes of data between the ground and GEO satellites. To address this increasing need (several Tb/s in the coming decades [1,2]), optical technologies are very competitive candidates. Their most cited advantages are a regulation-free spectrum, the technological maturity of the optical components for the ground segment (detectors, MUX/DEMUX, optical amplifiers) owing to the 40 years of development in fibered technologies, and intrinsically more secured communications due to extreme directivity.

However, ground-to-satellite laser links are challenging because the optical beam has to propagate through a few tens of kilometers of atmosphere, which leads to two major issues: cloud coverage and optical turbulence [3]. For the first one, several studies [4,5] demonstrate that the joint use of a dozen ground stations disseminated in Europe enables one to overcome the potential occultation of the line of sight (LOS) caused by nebulosity (site diversity concept). Yet the second issue, i.e. atmospheric turbulence, remains; indeed, the air index fluctuations lead to a notable decrease in the mean received power, and also to important temporal fluctuations of the received power around its mean, possibly leading to deep fades of the optical carrier. The future of very high throughput optical links between the ground and GEO satellites depends, therefore, on the ability to overcome turbulence-induced disruptions. Pre-compensation by adaptive optics (AO) has been identified as a game changer, as it could theoretically provide for the uplink by the additional margin necessary to secure the link budget at all times [6].

The principle of AO pre-compensation is to analyze the phase distortion on a beam coming from the satellite (the downlink beam), and then pre-distort the wavefront of a beam emitted from the ground to the satellite (the uplink beam), using a deformable mirror (DM). The reciprocity principle ensures that both downlink and uplink are impacted by the exact same phase distortion if the direction of analysis is the same as the direction of correction, and if the turbulence is “frozen” during the round-trip of light through the turbulence layers, as long as there are no differential aberrations due to the turbulence and the optical setup for both paths [7,8]. However, because of Earth and satellite rotation, and round-trip flight time of light, the directions of the downlink and the uplink are separated by about an $18.5\ \mu\text{rad}$ point-ahead angle (PAA) in the GEO case [9]. This leads to the main limitation of the AO pre-compensation performance: anisoplanatism, since the typical order of magnitude of the turbulence correlation angles is about $10\ \mu\text{rad}$, i.e. of the same order of magnitude as the PAA.

AO compensation has been tested on real downlink beams in both LEO [10] and GEO [11] cases; however, to our knowledge, to date no real AO pre-compensated ground-to-satellite feeder link has ever been tested. Some experiments have implemented tip-tilt only pre-compensation for links from ground to GEO satellites [12], or even toward the Moon [13], generally using multi-aperture systems; however, higher order correction has never been implemented. For now, efforts have been devoted to laboratory and field demonstrations. For example, DLR has developed a test-bed within the framework of the project “Terabit Throughput Satellite Technology Project” (THRUST). The objective is the demonstration of a 10 km, near-ground Tbit/s link with tip-tilt pre-compensation in conditions representative of ground-GEO uplinks. Objectives and preliminary results are presented in [14], and field trials were conducted in the late 2010s. The gain brought by tip-tilt only and AO pre-compensation has been demonstrated [15] but without taking into account the effect introduced by the PAA.

An implementation of AO pre-compensation with PAA consideration is presented in a laboratory experiment [16] and an outdoor demonstration close to the ground over a horizontal propagation distance of 1 km [17,18]. In [18], the authors show a gain when using an AO pre-compensation in terms of mean received intensity and smaller residual fluctuations, that decreases for a higher PAA. More recently, TNO and DLR have performed a 10km experiment, OFELIA [19], which is very similar to the FEEDELIO experiment presented here. They collected data for different PAA and different AO correction levels (number of corrected modes). They show a gain in the link budget taking into account the irradiance and scintillation of the received signal. Although these studies constitute an interesting first step in the demonstration of AO pre-compensation, none of them compares experimental performance to theoretical models.

The goal of this paper is to provide an in-depth analysis of the experimental results obtained during the FEEDELIO experiment, in order to assess the feasibility and relevance of AO pre-compensation for GEO feeder links (GEO-FL). The aim is to evaluate the robustness of such systems over a wide range of turbulence conditions, as well as to improve our understanding of the impact of turbulence on the system performance by comparison to models, with an emphasis on the anisoplanatism error induced by the PAA. This way, we will be able to comment on the representativeness of experiments such as FEEDELIO compared to the operational case on the sky. Please note that the temporal aspects are outside of the scope of this paper and will be evaluated in future studies.

The paper is organized as follows: we first present the FEEDELIO experiment in section 2. We then analyze the variations of signal statistics with regard to turbulence profiles that were inferred from AO data, and compare them to theoretical values obtained with ONERA’s models in section 3. Lastly, we conclude this work by discussing the representativeness of such slant path experiments compared to actual ground-GEO links in section 4.

2. FEDELIO experiment

2.1. Experiment overview

The FEDELIO experiment took place in Tenerife during two sessions: the first one in April 2019, the second one in October 2021. Unless otherwise stated, the results presented here come from the first campaign, which aimed to perform a ground experiment that demonstrated turbulence pre-compensation by AO under conditions representative of a GEO-FL scenario. In practice, the objective was twofold: to demonstrate the capacity of AO to increase the average transmitted power and drastically reduce the power fluctuations of the optical signals over a wide range of turbulence conditions; and to identify among them the conditions that were the closest to a real GEO-FL. The optical signal was not modulated, since the goal of this work was to emulate the effect of the pre-compensated atmospheric channel on the optical carrier.

The system consists of two terminals on both ends of a 13 km slant path with 5° elevation, as shown in Figs. 1 and 2:

- the Ground Terminal Breadboard (GTB) emulates an Optical Ground Station (OGS) equipped with a Shack-Hartmann (SH) wavefront sensor (WFS) that analyzes the phase of the downlink beam, and with a DM that allows pre-compensation of the uplink beam. It is also equipped with a downlink single mode fiber injection path, as well as a focal plane camera (FPC) to control visually, in real time, the quality of correction. It is installed on the southern pillar of the ESA OGS, at Tenerife observatory.
- the Satellite Terminal Breadboard (STB) emulates a satellite emitter and receiver, and records time sequences of the received signal on the uplink beam, as a function of adjustable PAA. The STB is installed at the Teide cable car station. It consists in two modules on a rail:
 - the “on-axis module”, which is set at a fixed position. It serves as a satellite transmitter and a reference downlink beam for wavefront sensing, as well as a satellite receiver in the absence of PAA.
 - the “off-axis module”, which serves as a satellite receiver. Motorized, its position could be controlled remotely in order to emulate variable PAA values.

The GTB consists of a 35 cm diameter telescope with a 24% central obscuration, coupled with an AO bench with a 1.5 kHz sampling frequency, a SH WFS with 8x8 subapertures, and a DM with 11x11 actuators, correcting either tip-tilt only, or about 50 modes of aberrations in “full correction” mode. On the STB side, the (non-modulated) received optical signal is collected through a pinhole-like pupil (1.7 mm diameter while the beam is about 10 centimeters wide), and recorded at 20 kHz. This sampling frequency was chosen to be well above the coherence frequency of turbulence (typically 100Hz to 1kHz), so that the turbulence induced fluctuations are well sampled. The optical sources’ wavelengths are 1.55 μm for the downlink and 1.62 μm for the uplink; their output power is chosen to get high SNR ($SNR \approx 30$). This design was chosen to be able to face a large panel of turbulence conditions, as these vary very significantly over time due to the proximity of the ground on this LOS. It was also chosen to be as representative as possible of a GEO-FL when meeting adequate turbulence conditions, as was explained in detail in [20]. This aspect will be discussed here in section 4. More information on the experiment itself can be found in [21,22].

2.2. Turbulence characterization

The key limitation factor of AO for GEO-FL with large diameters is anisoplanatism. This phenomenon is highly dependent on the turbulence distribution along the LOS, so it is of critical importance to be able to assess the C_n^2 profile. Throughout this article, we will thus discuss

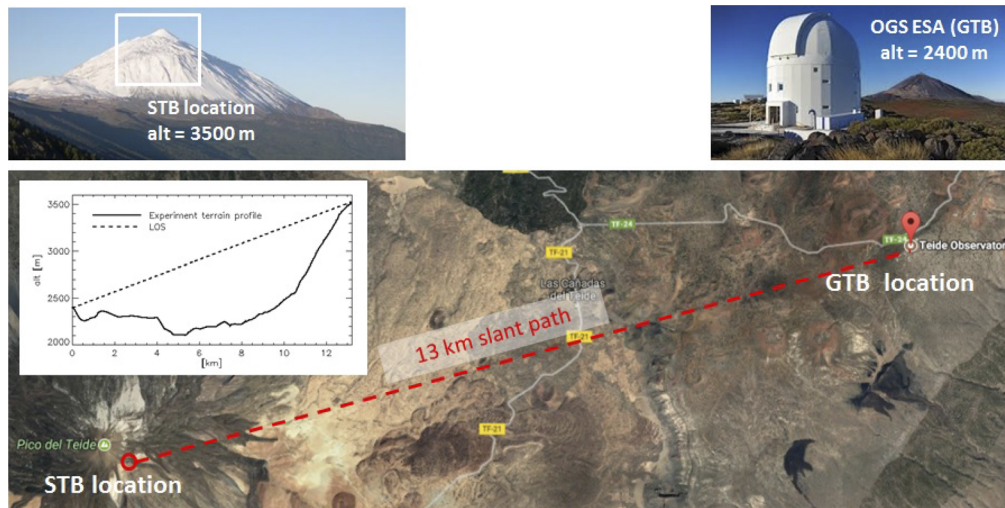


Fig. 1. Overview of the FEEDELIO experiment line of sight. The adaptive optics pre-compensated GTB is installed in the dome of ESA OGS (on the right), while the STB is on the cable car facility near the top of the Teide.



Fig. 2. On the left: the GTB, inside the dome of ESA OGS. In the middle: the STB, at the Teide cable car station. On the right, a face view of the STB, showing close-ups of the on-axis and off-axis modules. The downlink beam is in blue, while the uplink beam is in red.

turbulence profiles, but also integrated turbulence parameters, such as Fried parameter r_0 , scintillation as variance of the log-amplitude σ_χ^2 , and turbulence correlation angle θ_0 [23–26].

Since turbulence conditions are highly dependent on local environmental configuration (local wind flows and surface emissivity), the best way to properly assess turbulence impact on the LOS is to extract the Cn^2 profile directly from data provided by the AO loop concomitant to the acquired AO compensated signal. The method exploited here was proposed 15 years ago [27] and was validated under similar turbulence conditions [28]. It relies on the exploitation of phase and amplitude spatial correlations registered by a Hartmann-Shack WFS and a data inversion process under the small perturbations approximation.

Typical turbulence profiles computed from SH data and used in this study are plotted in Fig. 3. We can see that there are strong layers of turbulence at the half-way point, despite the high height of the LOS at this point (above the Teide caldera, see Fig. 1), which leads to strong scintillation conditions.

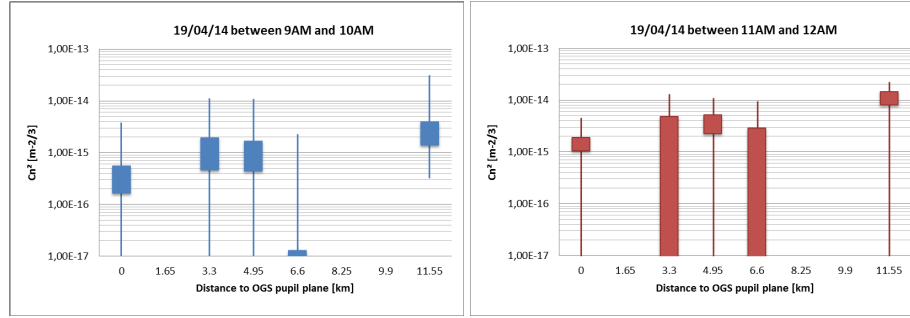


Fig. 3. Example of estimated turbulence profiles on the OGS-Teide LOS, for the morning of April 14th. The boxes delimit the lower and upper quartiles, while the lines extremities delimit the minimum and maximum values. The graph on the left is early morning, with mild turbulence conditions, while on the one on the right corresponds to late morning, with stronger turbulence conditions.

With these retrieved turbulence profiles, we calculated the values of r_0 , σ_χ^2 , and θ_0 using Rytov formulas in the spherical wave case [24], that are recalled below:

$$r_0 = [0, 423 \left(\frac{2\pi}{\lambda} \right)^2 \int_0^{z_{max}} Cn^2(z) \left(1 - \frac{z}{L} \right)^{\frac{5}{3}} dz]^{-3/5} \quad (1)$$

$$\sigma_\chi^2 = 0, 5631 \left(\frac{2\pi}{\lambda} \right)^{7/6} \int_0^{z_{max}} Cn^2(z) \left[z \left(1 - \frac{z}{L} \right) \right]^{5/6} dz \quad (2)$$

$$\theta_0 = [2, 91 \left(\frac{2\pi}{\lambda} \right)^2 \int_0^{z_{max}} Cn^2(z) \left[z \left(1 - \frac{z}{L} \right) \right]^{5/3} dz]^{-3/5} \quad (3)$$

where λ is the wavelength, z the distance to the ground aperture, and L the overall distance along the line of sight. All the turbulence integrated parameters used in this paper were calculated through this method.

However, we encountered cases with saturated turbulence, for which Rytov formulas are not applicable. Therefore, when discussing comparison to performance models, we will limit ourselves to cases where $\sigma_\chi^2 < 0.3$. Examples of evolution of r_0 and σ_χ^2 for the data set of Fig. 3 is given in Fig. 4. In the σ_χ^2 plot, we also show the intensity fluctuations measured in SH subapertures, σ_{ISH}^2 , which should be equal to four times the average Rytov log-amplitude fluctuations in a subaperture, $\sigma_{\chi_d}^2$, calculated from our estimated profiles. We can see in this graph that despite the high level of perturbations between 10 AM and noon, estimated and measured scintillation indexes are still very close, which strengthens our confidence in the robustness of our profile estimation throughout the experiment.

Note that in practice, scintillation speckles in this scenario are large on the wavefront sensor, and $\sigma_{\chi_d}^2$ is almost the same as the punctual variance of the log amplitude, σ_χ^2 , that will be used further on.

2.3. Signal statistics metrics

In this paper, we analyze theoretical and experimental performance with regard to turbulence properties. For this purpose, we have chosen to use simple metrics in order to compare orders of magnitude over a large panel of turbulence conditions: mainly, mean signal $\langle S \rangle$ and signal standard deviation $\sigma_S / \langle S \rangle$, where S is the optical signal received in the on-axis or off-axis STB receiver, i.e. the telecom optical carrier signal. In order to display statistics that are independent

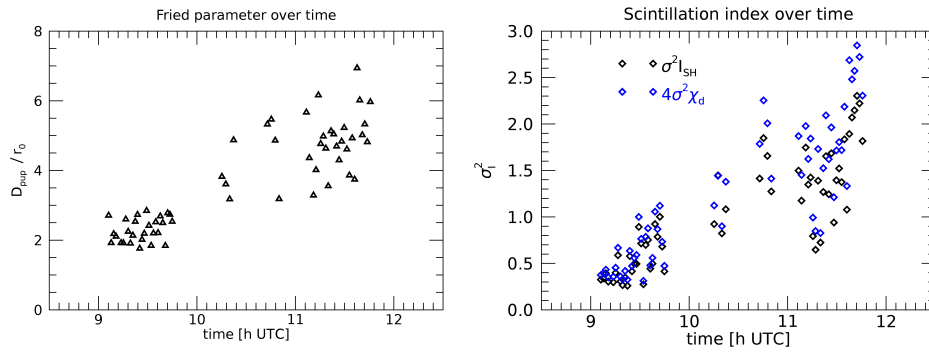


Fig. 4. Evolution over time of Fried parameter r_0 and log-amplitude variance $\sigma_{\chi_d}^2$ in subpupil, for the same set of data as Fig. 3. Local time in Tenerife is UTC+1. That day, the sun rose at 6:42 AM UTC, and set at 19:28 AM UTC.

of the signal power or pupil geometry, we will always plot normalized signal values, i.e. $\langle S \rangle / S_0$, where S_0 is the signal with no pointing error and no turbulence.

S_0 was estimated through link budget calculations such as the one depicted in Table 1. All of the terms of that link budget were calculated (antenna gains [29]) or calibrated (emitted and received power, optical transmissions, and static aberration losses) with the exception of the atmospheric transmission at $1.55 \mu\text{m}$. For that term, a reference value was estimated from the link budget in a very low turbulence case ($r_0 > 80 \text{ cm}$), and then atmospheric transmission variations were estimated from variations of the Power in the Bucket (PIB) measured on the focal plane camera (FPC) at GTB. However, during the experiment, we encountered some issues with background signal subtraction on the FPC, and STB orientation, which led to uncertainties of around 10% on the S_0 value at a given time. We do not represent the uncertainty bars on all the figures of the paper for clarity reasons, but this is the main source of experimental uncertainty.

Table 1. Experimental vs diffraction limited theoretical link budget

Uplink link budget - on axis - low turbulence - AO loop closed			
Name		unit	value
GTB	Optical output power (cw)	dBm	8.6
	Tx Optical Antenna Gain, diffraction limited	dB	115.3
	Tx Optical Transmission	dB	-0.5
	Tx Static aberration losses	dB	-0.2
Channel	Atmospheric transmission	dB	-0.5
	Loss free space propagation up	dB	-220.4
STB	Rx Optical Antenna Gain, w multimode fiber	dB	70.9
	Rx Optical Transmission	dB	-1
Theoretical mean received power, diffraction limited		dBm	-27.8
Experimental mean received optical power		dBm	-27.7

2.4. Bidirectional performance, bench optical quality

Typical on-sky long exposure Point Spread Functions (PSFs) on the downlink, captured on GTB side by the FPC, are shown in Fig. 5, reading from left to right: in open loop, tip-tilt only correction, and AO correction. The PSFs on the upper part of the figure were taken in early morning, with mild scintillation conditions ($\sigma_{\chi}^2 \approx 0.05$). The ones on the lower part were taken a few hours later, with stronger scintillation conditions ($\sigma_{\chi}^2 \approx 0.4$), but the loop remained very stable. These PSFs show a qualitatively satisfying AO correction.

An example of a one-second time series, recorded at 20 kHz on the uplink beam at STB, with no PAA, is shown in Fig. 6. In that example, even though scintillation is pretty strong ($\sigma_{\chi}^2 \approx 0.3$),

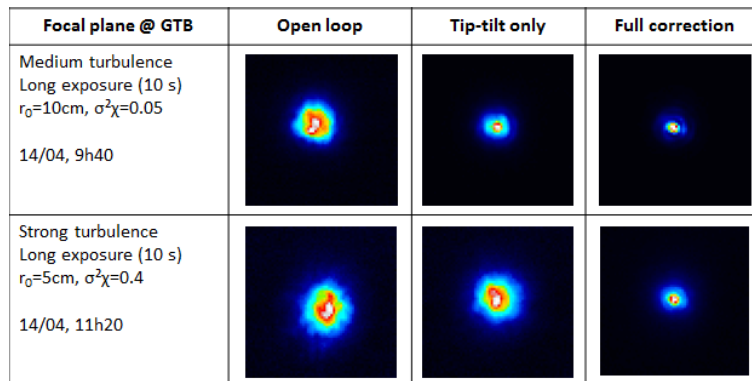


Fig. 5. Typical long exposure downlink PSFs obtained on the focal plane camera of GTB, showing the beam quality of the downlink beam, for medium and strong scintillation. This dataset is the same as the one shown in Fig. 3, 4, and 9, and later in section 3.2.

the improvement of signal statistics thanks to AO is evident compared to when there was either no correction at all or only tip-tilt correction. Note that even though tip-tilt correction is already a noticeable improvement in terms of mean signal, deep fades still occur while fades disappear from the AO-compensated signal.

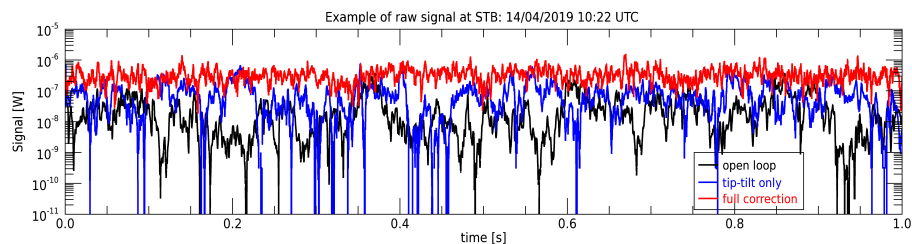


Fig. 6. Example of experimental signals acquired at STB with no PAA, for open loop operation (in black), tip-tilt only correction (in blue), and full AO correction (in red). NB: These time series are a breakdown of the 10:22 series of Figs. 4 and 10.

Figure 7 shows an example of partial reciprocity between the uplink and the downlink we obtained with a tip-tilt only corrected signal. Here, the uplink and downlink signals are recorded in a strictly monostatic configuration, sharing the exact same pupils for both emission and reception. The only differences with perfect reciprocity are non-common-path aberrations (NCPAs), including mispointing, differential in wavelength, and detection noise on PIN detectors. In this example, the correlation coefficient over the 10 second time series is 95%, which is consistent with the 0.3 radian of NCPAs that were measured on the bench, as explained in [30].

Long exposure beam profiles recorded at STB in case of low turbulence (as in Fig. 8), allows us to measure diffraction-limited divergence of the uplink on-axis beam, showing that pre-compensation works as expected.

The bidirectional link is necessary to assess the value of NCPAs and radiometric calibration. The focus of this paper is, however, the pre-compensation of the uplink beam. Therefore, hereafter, static aberrations are compensated on the uplink, and what is called “signal” is the uplink optical carrier signal, measured by the PIN detectors on the STB side or calculated with models.

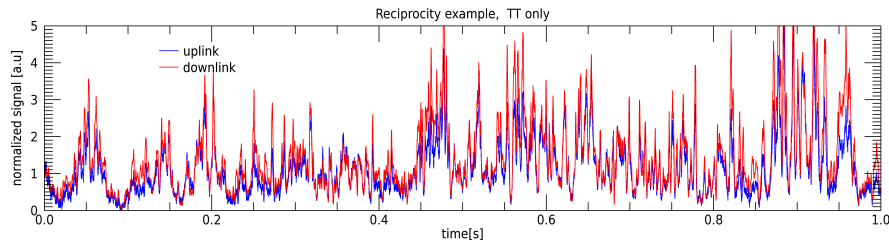


Fig. 7. Example of partial reciprocity between the downlink and the on-axis uplink, in a strictly monostatic configuration. This specific sequence considers a tip-tilt only correction, and has a correlation coefficient of 95% over a 10 second time series.

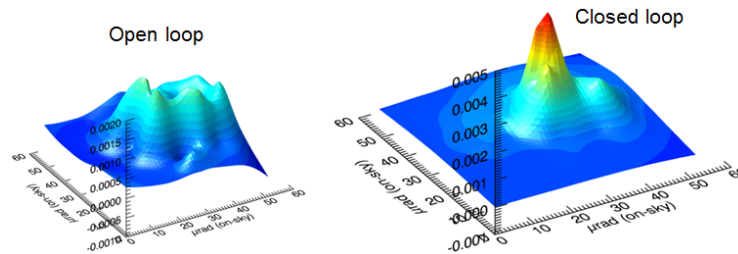


Fig. 8. Example of long term exposure PSFs at the STB plane without AO (on the left) and with AO closed loop (on the right), obtained through spiral scanning of the beam in front of the STB PIN detector. Turbulence conditions are $r_0 = 10$ cm, $\sigma_\chi^2 = 0,06$.

3. Experimental AO performance on the uplink, and comparison to theory

3.1. Approach

The main objective of the experiment is to demonstrate the feasibility of AO pre-compensation under highly variable turbulence conditions, such as would be encountered during 24-hour operation of a feeder link system, and to study its limitations under propagation conditions relevant to a GEO-FL. A secondary goal of this experiment is to generate statistical quantities of raw signal under conditions similar to those of a GEO-FL and use them to validate performance models.

Our approach is thus the following: we record sequences of 10 seconds of experimental raw optical signal with the corresponding Real Time Computer (RTC) data, i.e. SH data such as slopes and aperture intensities, and commands of the DM. Then we post-process the SH data in order to calculate an estimated turbulence profile as described in paragraph section 2.2 and use this profile as our input in our models in order to compute theoretical signal statistics that we can then compare to the corresponding experimental signal statistics.

Two ONERA models were used for cross-validation in this study: the SAOST model (for “Simplified Adaptive Optics Simulation Tool”) and the PILOT model (for “Propagation tool for Imaging and Laser through Optical Turbulence”). Both models take into account the impact of the spherical wave propagation due to the finite distance of the link in the FEDELIO experiment.

3.1.1. SAOST model

The SAOST model belongs to the family of codes based on the exploitation of the statistical properties of the field after propagation, such as the code FAST [31]. The main difference is that FAST uses Fourier formalism, while SAOST is based on the Zernike modal decomposition of the

phase. Description of SAOST can be found in previous work, such as [32], [33], or [34]. The main principles are summarized below.

The SAOST model is based on analytical models associated to a Monte-Carlo approach that allows to obtain random draws of complex amplitude ψ_k in the ground pupil aperture (where k indicates the occurrence of the draw):

$$\psi_k(\mathbf{r}) = A e^{\chi_k(\mathbf{r})} e^{i\phi_k(\mathbf{r})} \quad (4)$$

The model assumes that the statistics of the phase ϕ_k and log-amplitude χ_k in Eq. (4) are uncorrelated. The χ_k values are obtained simply through random draws following the well-known statistics of χ in the Rytov regime [24], while the ϕ_k values require a bit more work: in case of AO correction, the ϕ_k values are draws of the residual phase, i.e. the difference between the turbulent phase and the phase corrected by the deformable mirror. In SAOST model, AO correction simulation is based on a detailed modal AO error budget, where the phase is decomposed onto a finite set of Zernike's polynomials Z_i with Noll's definition [35]:

$$\phi_k(\mathbf{r}) = \sum_{i=2}^{i_{max}} a_{i,k} Z_i(\mathbf{r}) \quad (5)$$

where i_{max} is the index of the last Zernike mode used to describe the phase perturbation, where we have excluded Z_1 , the piston mode.

The $a_{i,k}$ coefficients are calculated through random draws, considering gaussian distributions characterized by the modal variance $\sigma_{a_i,res}^2$ of the residual phase, $\sigma_{\phi,res}^2$:

$$\sigma_{\phi,res}^2 = \sum_{i=2}^{i_{max}} \sigma_{a_i,res}^2 \quad (6)$$

The $\sigma_{a_i,res}^2$ values are calculated as follows, considering that $i_{max,corr}$ is the index of the last corrected Zernike mode:

- For $i > i_{max,corr}$: the modes are not corrected by AO (it's the "fitting error") and are thus directly the modal variance of the turbulent phase, that can be deduced from the D_{pup}/r_0 value through Noll formulas [35].
- For $i \leq i_{max,corr}$, the modal residual variances are obtained by adding several contributors:
 - the aliasing error, which is supposed to be 35% of the fitting error, with modal distribution given by Refs. [36] and [37],
 - the temporal error term, which is the result of the summation of the residual modal variance due to temporal error :

$$\sigma_{tempo}^2 = \sum_{i=2}^{i_{max,corr}} \int_0^{\infty} RTF(f, f_s) PSD_i(f) df \quad (7)$$

where PSD_i is the temporal power spectral density of the turbulent phase for the Zernike index i , which takes into account the wind profile [38]; and RTF is the closed loop rejection transfer function. We consider here a 2-frames-delay integral controller with 0.5 gain [39], f_s being the sampling frequency of the control loop.

- and finally the anisoplanetic error, which is calculated thanks to Zernike modal angular correlations given in Refs. [40] and [41].

Once random draws of ϕ_k and χ_k have been calculated, SMF coupling can be deduced by calculation of the square modulus of the overlap integral Ω between the wave's complex amplitude and the Gaussian mode of the fiber (or of the local oscillator laser), M_0 , on the support of the receiver's aperture, P:

$$\Omega_k = \frac{\langle \psi_k | M_0 \rangle_P}{\sqrt{\langle \psi_k | \psi_k \rangle_P \langle M_0 | M_0 \rangle_P}} \quad (8)$$

Statistics of the loss of signal due to turbulence only can then easily be calculated for each draw:

$$\frac{S_k}{S_0} = \frac{|\Omega_k|^2}{|\Omega_0|^2} \quad (9)$$

where Ω_0 is the overlap integral in case there's no turbulence (i.e. when ϕ and χ are null), whose value is well known, and takes into account the central obscuration of the telescope. [29].

This model allows us to perform quick sensibility studies and to compute statistical series with a high number of occurrences, for a good statistical convergence. With those series we can derive theoretical mean values and standard deviations of the signal, as used in sections 3.2 and 3.3, as well as cumulative distribution functions (CDF), such as those used in section 4. However, it is limited to the Rytov regime and does not include a precise description of AO components, as the input parameters are the number of corrected Zernike aberration modes, sampling frequency, delay, PAA, and pupil diameter. It does not take into account the exact WFS geometry and noise (i.e. a high SNR in the WFS subapertures is assumed).

3.1.2. PILOT model

The PILOT model is an End-to-End (E2E) model, based on the classic split-step algorithm [42], and has been developed at ONERA for more than two decades. It is similar to other codes that can be found in literature, such as [43], [44], or [45]. It models turbulence effects with Fresnel propagation through random screens. An AO correction simulator, also developed by ONERA, AOST ("Adaptive Optics Simulation Tool"), uses the outputs provided by PILOT to simulate the closed loop operation, based here on an integrated controller with a two-frames delay. The simulator is based on a diffractive modeling of the WFS and a discrete time representation of the correction, here based on Zernike modes. The obtained pre-compensated uplink fields are then reinjected into the PILOT propagation tool to assess the uplink power deposited in the satellite plane with PAA - or in the STB plane in the case of FEEDELIO. Being an E2E model, PILOT + AOST can also provide correlated time series for the uplink at the cost of much longer simulations compared to SAOST. In addition to that, it is able to take into account perturbations beyond the Rytov regime, which are out of the reach of the SAOST tool. The quantities provided by the PILOT + AOST simulations are thus more accurate to a certain extent, but the simulations are so costly that we don't reach perfect statistical convergence. Note that the "PILOT" data mentioned further on this paper were computed so as to obtain two-seconds time series.

3.2. Uplink pre-compensation performance without PAA

Figures 9 and 10 show the same experimental time series statistics without PAA, plotted versus turbulence integrated parameters (Fig. 9), and versus time (Fig. 10). These were acquired during a 3 hour experiment session on April 14, 2019, under a wide range of turbulence conditions.

Figure 9 shows that whatever the strength of turbulence conditions, the AO correction mitigates the perturbations very efficiently: gains of around 10x in the mean coupled flux were obtained between the open loop and closed loop (left figure), and signal fluctuations were noticeably reduced (right figure). There is also a clear gain in compensating for radial orders higher than tip-tilt, even though tip-tilt compensation already provides a substantial improvement in signal statistics.

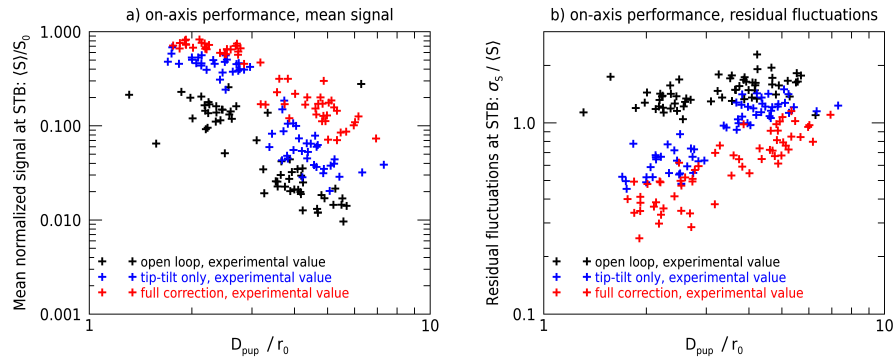


Fig. 9. Experimental performance as a function of the ratio between pupil diameter D_{pup} and Fried parameter r_0 (on-axis uplink data acquired on April 14, 2019, in the morning). Left: mean coupling ratio. Right: residual signal fluctuations. Same set of data as for Figs. 3 and 4.

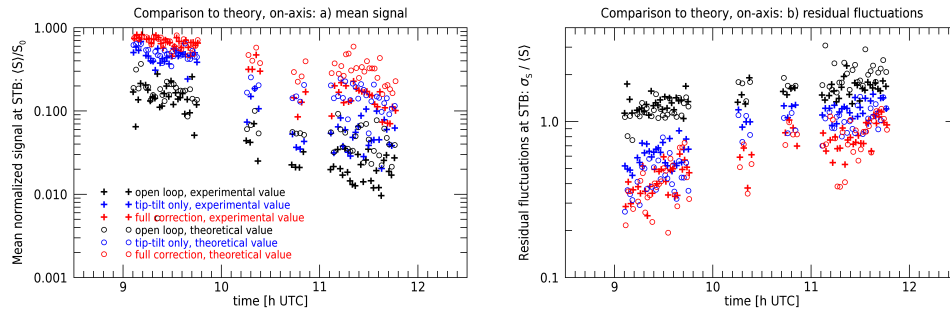


Fig. 10. Comparison between experimental and SAOST theoretical performance as a function of time (on-axis uplink data acquired on April 14, 2019, in the morning). From left to right: mean normalized signal, residual signal fluctuations. The corresponding r_0 and σ_χ^2 are given in Fig. 4.

Figure 10 shows how turbulence conditions became gradually stronger during the session, and compares the experimental time series statistics to theoretical signal moments calculated with SAOST, using the approach described in section 3.1. Corresponding integrated turbulence parameters, i.e. D_{pup}/r_0 and scintillation index σ_χ^2 , are those of Fig. 4. This figure shows that the results obtained by our prediction models are quite close to what was obtained experimentally, though the consistency is much better for early morning values (between 9 and 10 AM), and worse in late morning, when the turbulence becomes stronger.

This can be explained by the fact that the turbulence went into the strong perturbation regime, with scintillation conditions beyond the Rytov regime ($\sigma_\chi^2 > 0.3$), as can be seen from the scintillation index displayed in Fig. 4. This is expected considering the turbulence profiles we met, with a strong turbulence layer in the middle of the LOS (cf. Figure 3). In these conditions, the scintillation strongly affects the SH wavefront measurements: the signals received by some subapertures are saturated while others are very weak, as can be seen in Fig. 11. Moreover, our RTC is not optimized for such conditions, as the slope measurement algorithm is not the most robust to scintillation (center of gravity calculation with the same threshold for all the subapertures). Moreover, since the SAOST model is presently limited to the Rytov regime (cf. section 3.1), it is less accurate in the strong perturbations regime, although it delivers the

right orders of magnitude, as was discussed in more depth in [46]. Still, despite those strong scintillation conditions, the loop remained stable and robust.

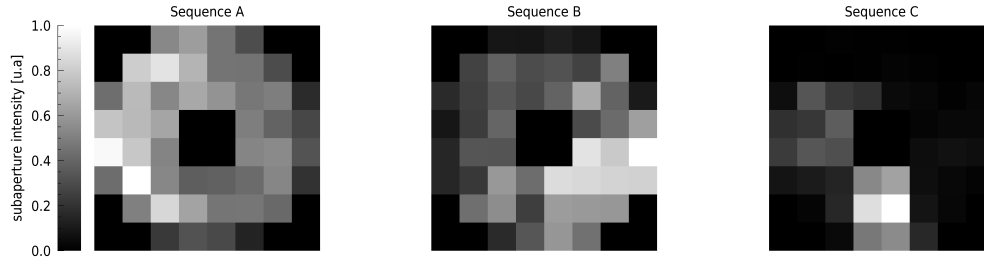


Fig. 11. Example of SH averaged received intensity per subaperture on one single frame, for very low scintillation (left), medium scintillation (middle), and strong scintillation (right), i.e. respectively from Sequence A, B and C, that are studied in section 3.3. Note that a threshold value is applied on these experimental data, hence a value of zero means the received intensity is below the threshold set by the user.

3.3. Uplink pre-compensation performance with respect to PAA

We discussed in the previous paragraph that our models showed good accuracy without PAA. Now we will assess the impact of PAA-induced anisoplanatism on pre-compensation performance and validate our models based on these experimental data. Note that hereafter, the analysis will be focused on high order mode correction for the sake of concision, but similar conclusions could be drawn for tip-tilt only, which is a particular case of low order mode AO.

To record signal statistics as a function of the PAA, 10 seconds time series are recorded successively for four different positions of the off-axis STB module, corresponding to PAAs going from 3 to 50 μrad . In this article, we select three sequences for illustration purpose: Sequence A has very weak anisoplanatism, Sequence B mild anisoplanatism, and Sequence C strong anisoplanatism. They were taken on different days and nights, and were chosen because they correspond to very different turbulence profiles while still showing scintillation levels within the range of validity of our turbulence profile estimation model ($\sigma_\chi^2 < 0.3$). The turbulence profiles averaged over each of these three sequences can be seen in Fig. 12, while their corresponding integrated parameters and time stamps are shown in Table 2. Corresponding examples of SH averaged received intensity per subaperture are depicted in Fig. 11.

Table 2. Turbulence integrated parameters corresponding to the turbulence profiles depicted in Fig. 12 at 1.62 μm , and computed in spherical wave

Sequence name	Time and date	r_0	σ_χ^2	θ_0
Sequence A	2019/04/13 at 11:03 PM	89 cm	0.014	46.7 μrad
Sequence B	2019/04/12 at 10:21 AM	12 cm	0.19	18.5 μrad
Sequence C	2019/04/14 at 11:31 PM	15 cm	0.26	7.8 μrad

One second of raw acquisition of sequence B is plotted in Fig. 13: we can see qualitatively how the number and depth of fades increases with the PAA, even reaching statistics close to the open-loop operation depicted in Fig. 6. This illustrates the loss of performance induced by anisoplanatism.

The first two moments of the signals recorded in the three sequences are plotted in Fig. 14 (solid lines). The theoretical values estimated by SAOST and PILOT models are also depicted in dotted and dashed lines. As explained in section 3.1, the effect of noise and scintillation on SH

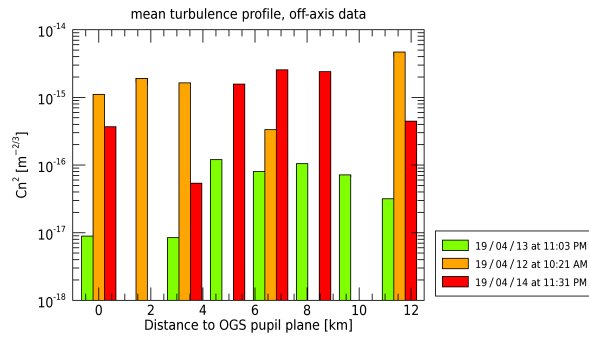


Fig. 12. Mean turbulence profiles retrieved from RTC data, corresponding to Fig. 14 data, with the same color code : Sequence A in green, Sequence B in orange, and Sequence C in red.

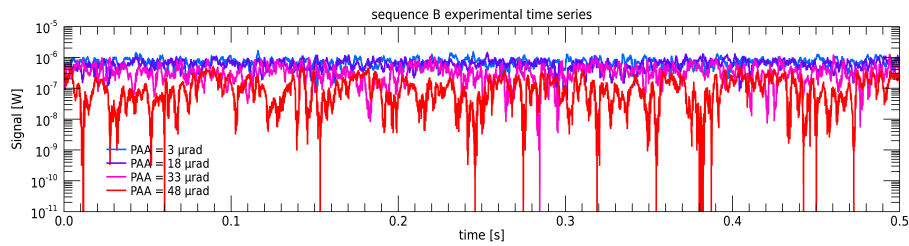


Fig. 13. Example of uplink experimental signal acquired at STB for different PAA values. The sequence shown here is the “sequence B” discussed further in this paper.

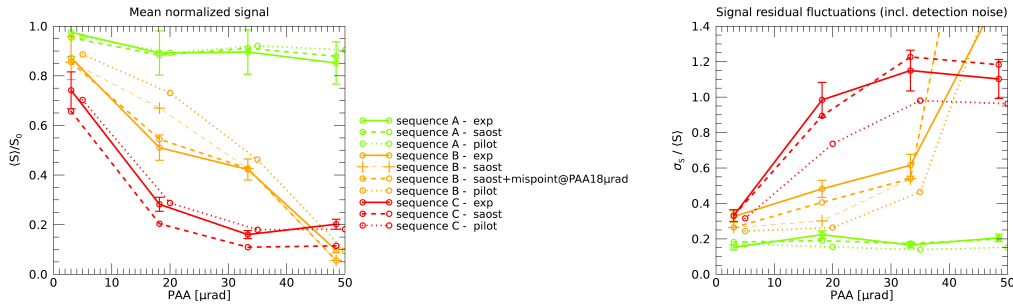


Fig. 14. Off-axis performance for three sequences with varying degrees of anisoplanatism. Experimental values (full AO) in plain lines, theoretical values with simplified model SAOST in dashed lines, theoretical values with end-to-end PILOT model in dotted lines. On the left: mean normalized signal as a function of PAA. On the right: residual fluctuations - due to both turbulence and detection noise on the PIN detector. Uncertainty bars are due to uncertainties on S_0 value, see section 2.3.

slope measurements and AO loop are neglected for these simulations; however, the detection noise on the PIN detector is taken into account. Each theoretical point is inferred from the turbulence profile estimated for the corresponding experimental value in the plot.

We can conclude from these figures and table that:

- Sequence A is a case with almost no turbulence: the Cn^2 of all the turbulence layers are around or below $10^{-16} \text{ m}^{-2/3}$, which leads to a r_0 much wider than the pupil diameter, a very low scintillation index, and very weak anisoplanatism (θ_0 around $50 \mu\text{rad}$). This

is a good reference case to check the accuracy of the pointing for all PAA values, as the evolution of performance must be stable with regard to PAA in case of very weak anisoplanatism. We can also see that both mean signal values (on the left of Fig. 14) and residual fluctuation values (on the right of the same figure) are extremely well predicted by both models.

- Sequence B is in fact the one that shows the smallest r_0 , i.e. the strongest phase fluctuations, but since the most turbulent layers are near the OGS, it shows less anisoplanatism and scintillation than Sequence C, where the most turbulent layers are in the middle of the LOS (cf. Figure 12). The AO is thus more performant in that case than for Sequence C. This illustrates that the real limitation in the performance of the experiment, and more generally of GEO-FL, is indeed anisoplanatism and not overall turbulence strength given by the r_0 .
- In the three sequences, despite being very different in nature, both models accurately predict variations of the first order moments of the signal with respect to the PAA. However, a few differences can be spotted. For mean values, PILOT seems to be more accurate, especially as the turbulence gets stronger. This can be explained by the fact that this model takes into account more error terms and depicts more accurately the AO components and loop. However, SAOST seems more accurate for residual fluctuations estimation, which can be explained by the lack of statistical convergence of PILOT time series, as explained in section 3.1. More generally, the differences between the experiment and the models can be explained by 1) uncertainties in the estimation of the profiles due to uncertainties in the measurement of both the slopes and intensity by the SH and lack of statistical convergence; 2) residual pointing errors that we did not take into account in our models; and 3) the non-consideration of scintillation-induced WFS errors in our models.
- Regarding mispointing, Sequence B shows at first sight a noticeable difference between the models and the experiment for one PAA value, $18 \mu\text{rad}$. However, this sequence was recorded at the beginning of the experimental campaign when we still had some problems with the off-axis motion of the STB module, which was sometimes slowed down by mechanical problems; it is therefore very likely that the difference is due to mispointing. Indeed, simulating a pointing error of $1 \mu\text{rad}$ in SAOST for this PAA point (and this point only) gives values closer to the experiment, both for the mean values and for the fluctuations, as shown through the orange dashed line in Fig. 14.

4. Discussion: application to GEO-FL

The good fit between the FEDELIO experiment results and our models shows a good understanding of how physical effects affect AO pre-compensation performance. Those models can thus be used with confidence in order to discuss the representativeness of the Tenerife LOS to emulate GEO-FL.

4.1. Reference scenarios for a GEO-FL

Both the SAOST and PILOT models evaluate the performance of a GEO-FL equipped with a given AO system and for a given turbulence profile along the LOS. The baseline scenarios must be chosen carefully in order to be representative of the typical performance that will be achieved once the AO-compensated GEO-FL are operational on the sky.

For AO configuration, we chose the same parameters as those used in [47], i.e. a 60 cm diameter emitter, and a 4.5 kHz AO loop, with 15 corrected radial orders. This configuration is representative of ONERA's future Optical Ground Station [48]. The reference PAA is $18.5 \mu\text{rad}$, and we used a Brufton wind profile of 30 m s^{-1} wind at 10 km layer, and 10 m s^{-1} near the ground [49].

Choosing reference turbulence profiles is, however, more difficult, since there is a lack of extensive open source databases of ground-to-space day turbulence profiles. We have therefore created reference scenarios called “MOSPAR” following the approach described in [47]. The idea is the following: we start from the hypothesis that the isoplanetic angle θ_0 and the Fried parameter r_0 are mostly independent from one another, since the former is determined mainly by the atmosphere at high altitudes (above 2000 m), while the latter depends mostly on the lower layers of the atmosphere. We also suppose that upper layers of the atmosphere don't change much during day and night. A statistical distribution of θ_0 is computed from a set of turbulence profiles measured at Paranal [50], while a statistical distribution of Cn^2 at ground level during day and night is computed from [51] and [52]. The behavior of Cn^2 for the low layers is deduced using a Monin-Obhukov similitude law, which allows the computation of the statistical distribution of the r_0 . We then choose θ_0 and r_0 according to the intensity of the turbulence we wish to represent. The values obtained for high and low layers are then brought together, resulting in the final hybrid turbulence profile.

As a baseline, we choose day profiles corresponding to turbulence conditions in the lower quartile of the available θ_0 and r_0 data, meaning that, for instance, for the MOSPAR7575 profile, 75% of our existing database values are better than this case study for both θ_0 and r_0 .

We considered here the following cases:

- MOSPAR5050: for weak turbulence (50th percentile)
- MOSPAR7575: for medium turbulence (75th percentile)
- MOSPAR9090: for strong turbulence (90th percentile)

These reference profiles are calculated for a 30° reference satellite elevation, and are shown in Fig. 15. Their corresponding integrated parameters are summed up in Table 3.

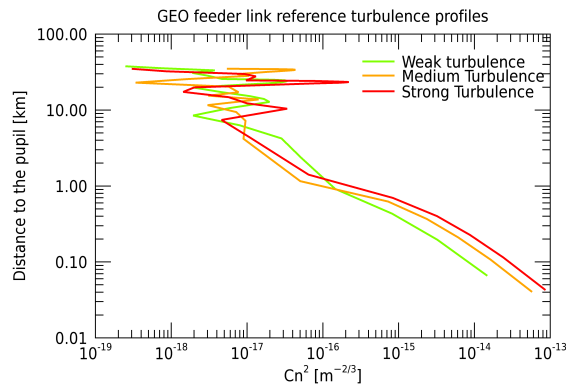


Fig. 15. MOSPAR reference profiles for a 30° elevation GEO satellite.

Table 3. Turbulence integrated parameters for MOSPAR reference profiles.

Profile name	Elevation	Wavelength	r_0	θ_0	σ_x^2
MOSPAR5050	30	1.55 μm	7.8 cm	11.3 μrad	0.035
MOSPAR7575	30	1.55 μm	5.4 cm	8.5 μrad	0.048
MOSPAR9090	30	1.55 μm	4 cm	6.8 μrad	0.079

4.2. Performance of an AO pre-compensated GEO-FL and comparison with FEEDELIO line of sight

In GEO-FL, the turbulence is located at the very beginning of the LOS, and the strongest turbulence layers are those close to the OGS; in particular, the altitude layers responsible for anisoplanatism and scintillation are expected to be several orders of magnitude lower than the layers close to ground level (cf. Figure 15). Moreover, turbulence can be considered significant only on the first few tens of kilometers, while the LOS we consider here is around 38,000 km long. In contrast, in slant or horizontal path experiments, the turbulence is distributed almost evenly, along the whole LOS. Moreover, horizontal and slant path experiments correspond roughly to a spherical wave scenario, which is known to be particularly sensitive to turbulence layers in the middle of the line of sight for both scintillation and anisoplanatism. It is thus expected to have difficulties to get turbulence conditions that are representative of a GEO FL for r_0 , θ_0 and σ_χ^2 at the same time.

The question is, then, to what extent are such experiments representative of GEO-FL? To answer this, theoretical CDFs of the signal, obtained with SAOST and for the aforementioned GEO-FL scenarios, are compared to the theoretical CDFs for FEEDELIO Sequences A, B and C; sets of results for both are plotted in Fig. 16 for PAA values corresponding to the FEEDELIO experiment, and in Fig. 17 for optimized PAA values. The corresponding values for the mean of the normalized signal and its standard deviation are summarized in Table 4.

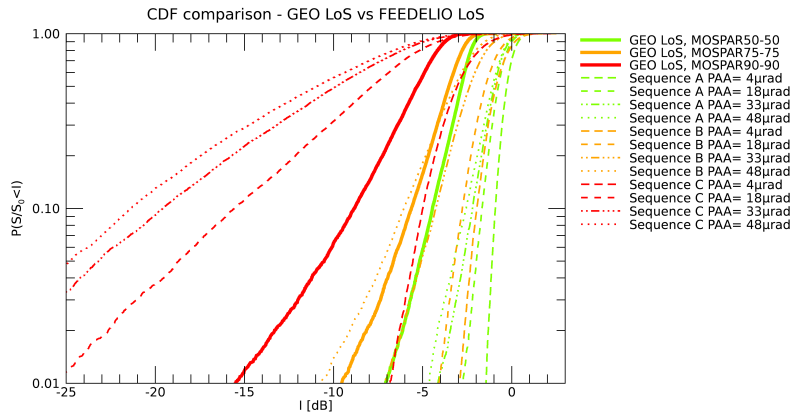


Fig. 16. Theoretical Signal CDF for a GEO-FL with 18.5 μ rad PAA, compared to the CDFs inferred from the turbulence profiles encountered during the FEEDELIO campaign (same sequences as section 3.3), with the PAA values of the experiment.

Table 4. Theoretical SAOST signal moments corresponding to the CDFs plotted in Fig. 17, for FEEDELIO profiles used as examples in this paper, and for a typical GEO-FL with 18.5 μ rad.

SAOST values		$\langle S \rangle / S_0$	$\sigma_S / \langle S \rangle$
FEEDELIO Sequence B	PAA= 35 μ rad	0.57	0.3
	PAA= 45 μ rad	0.49	0.35
FEEDELIO Sequence C	PAA= 9 μ rad	0.31	0.5
GEO-FL	MOSPAR5050	0.50	0.04
GEO-FL	MOSPAR7575	0.43	0.07
GEO-FL	MOSPAR9090	0.29	0.15

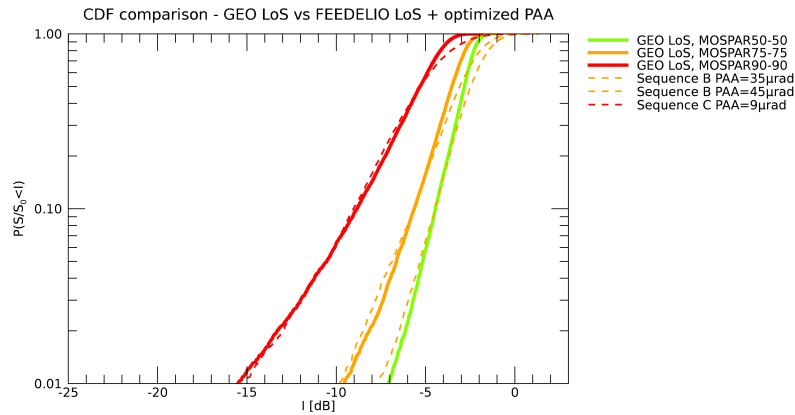


Fig. 17. Theoretical Signal CDF for a GEO-FL, compared to the CDFs inferred from the turbulence profiles encountered during the FEEDELIO campaign (same sequences as section 3.3), but this time with PAA values that could theoretically provide signal statistics very close to MOSPAR scenarios defined in section 4.1.

We can see in this table that in these examples, the moments of the signal differ significantly, even when the PAA is optimized to best fit low probability CDF values: the penalty on the mean power is of the same order of magnitude for the GEO-FL scenario and for FEEDELIO, but the second moments are expected to be significantly weaker for the GEO-FL case. However, if we consider that it's the weakest signal occurrences that are critical for the overall telecom performance, i.e. the CDF slope for low instant gain, we can still find a proper combination of slant path PAA and turbulence profile to emulate GEO-FL in variable scenarios, as shown in Fig. 17. However, in the slant path case, fluctuations are more due to scintillation than phase residuals, while in the GEO case the opposite is true. All in all, both phase and scintillation contribute to signal fluctuations, and it is the combination of the two that affects the optical carrier quality.

The great range of turbulence conditions encountered in slant path experiments can thus be seen as an opportunity to test systems over a very wide range of scenarios. Added to the capability to derive turbulence profiles and theoretical performance shown in this paper, it offers the possibility to choose from among all the scenarios the ones that are the closest to GEO-FL cases, and thus the most relevant, depending on a chosen criterion, such as CDF. The experimental PAA is also an interesting variable, as it allows us to “scan” over a wide range of signal distributions depending on the turbulence profile and the position of the receiver with regard to the emitter in the satellite emulator plane (the STB, in the case of FEEDELIO).

5. Conclusion and perspectives

These last years, there has been a raising interest in ground-to-GEO satellites optical very high throughput links, i.e. GEO feeder links, or GEO-FL. However, despite their potential, these applications have to overcome atmospheric turbulence, which requires the development of mitigation techniques, such as adaptive optics (AO). However, in the case of GEO-FL, AO performance is limited by the Point-Ahead Angle (PAA) induced anisoplanatism.

In this article, we presented the FEEDELIO experiment, whose goal was to evaluate the robustness of AO pre-compensation for GEO-FL over a wide range of turbulence conditions, as well as to improve our understanding of the impact of turbulence conditions on AO performance.

We first discussed the experimental performance without PAA by comparing experimental mean and standard deviation signal values, to values obtained by ONERA model SAOST. We

showed that the experimental performance is very close to theoretical models as long as the scintillation is not too strong. When scintillation conditions go above the Rytov regime, our model proves to be merely optimistic because it doesn't take into account the impact of scintillation on wavefront sensing. Still, the AO loop remains stable, despite very harsh scintillation conditions.

The impact of anisoplanatism on AO performance versus PAA was then studied by comparing experimental first order moments with theoretical values inferred from ONERA models SAOST and PILOT, through three examples corresponding to very different turbulence and anisoplanatism conditions, while still staying in the Rytov regime. It showed that we can predict the deterioration of the performance with regard to PAA with both our models with good accuracy.

Finally, these results gave us confidence in our capacity to model theoretical real ground-to-GEO signal statistics, which allowed us to discuss to what extent experiments such as FEEDELIO are representative of GEO-FL. We showed that signal standard-deviation due to turbulence residuals are much bigger for a horizontal or slant path experiment compared to a ground-to-space link. However, if we consider that Telecom performance is limited by low signal values, we can then find combinations of slant path experiment turbulence profiles and PAAs that lead to experimental CDFs close to GEO-FL CDFs for low probability values while keeping similar impact on the mean signal value. In that sense, these experiments are partially representative - and also, of course, a good "stress-test" for telecom systems, as the range of signal statistics that can be met in the span of only one day is very large.

Now that feasibility of AO-precompensation has been proven on slant paths experiments, the next step will be to test it on a real GEO-FL; to that purpose, ONERA is working on its own research ground station, FEELINGS [48]. But the main issue for AO-precompensation, as discussed here, remains anisoplanatism; however the performances shown here are not final, as it shows only expected performance for current state-of-the art AO. Research is ongoing to reduce the impact of anisoplanatism, through laser guide stars for instance [53], multi-emitter beams, or novel AO control methods.

Funding. European Space Agency; Office National d'études et de Recherches Aérospatiales.

Acknowledgments. This work has been performed in the framework of ESA's contract N°4000120300/17/NL/PS.

Our colleagues Bruno Fleury and Francis Mendez were essential to the success of this project, we thank them warmly and wish them a happy and rewarding retirement. Moreover, the FEEDELIO experiment would not have been possible without the very helpful contributions of the technical staff from Instituto Astrofísica de Canarias, Teide's National Park, and Teide's cable car station. The authors warmly thank them for their fruitful help and collaboration.

The authors also wish to thank J. Osborn of Durham University for kindly providing Paranal's Cn^2 profiles database.

Disclosures. The authors declare no conflicts of interest.

Data availability. Data underlying the results presented in this paper are not publicly available at this time but may be obtained from the authors upon reasonable request.

References

1. H. Hauschildt, C. Elia, H. L. Moeller, W. El-Dali, T. Navarro, M. Guta, S. Mezzasoma, and J. Perdignes, "Hydron: High throughput optical network," in *2019 IEEE International Conference on Space Optical Systems and Applications (ICSOS)*, (IEEE, 2019), pp. 1–6.
2. C. Volland, Z. Sodnik, J. M. Perdignes-Armengol, D. Alaluf, N. Vedrenne, and K. Nicklaus, "Towards optical data highways through the atmosphere," *Proc. SPIE* **10910**, 48 (2019).
3. Z. Sodnik, C. Volland, J. Perdignes, E. Fischer, K. Kudielka, and R. Czichy, "Optical feeder-link between esa's optical ground station and alphasat," *Proc. SPIE* **11852**, 1185218 (2021).
4. F. Lacoste, A. Guérin, A. Laurens, G. Azema, C. Periard, and D. Grimal, "Fso ground network optimization and analysis considering the influence of clouds," in *Proceedings of the 5th European Conference on Antennas and Propagation (EUCAP)*, (IEEE, 2011), pp. 2746–2750.
5. S. Poulénard, M. Crosnier, and A. Rissons, "Ground segment design for broadband geostationary satellite with optical feeder link," *J. Opt. Commun. Netw.* **7**(4), 325–336 (2015).
6. R. K. Tyson, "Adaptive optics and ground-to-space laser communications," *Appl. Opt.* **35**(19), 3640–3646 (1996).
7. J. H. Shapiro, "Reciprocity of the turbulent atmosphere," *J. Opt. Soc. Am.* **61**(4), 492–495 (1971).
8. J. H. Shapiro, "Point-ahead limitation on reciprocity tracking," *J. Opt. Soc. Am.* **65**(1), 65–68 (1975).
9. N. Martínez, L. F. Rodríguez-Ramos, and Z. Sodnik, "Toward the uplink correction: application of adaptive optics techniques on free-space optical communications through the atmosphere," *Opt. Eng.* **57**(07), 076106 (2018).

10. C. Petit, N. Védrenne, M.-T. Velluet, V. Michau, G. Artaud, E. Samain, and M. Toyoshima, "Investigation on adaptive optics performance from propagation channel characterization with the small optical transponder," *Opt. Eng.* **55**(11), 111611 (2016).
11. E. Fischer, T. Berkefeld, M. Feriencik, M. Feriencik, V. Kaltenbach, D. Soltau, B. Wandernoth, R. Czichy, J. Kunde, K. Saucke, F. Heine, M. Gregory, C. Seiter, and H. Kämpfner, "Development, integration and test of a transportable adaptive optical ground station," in *2015 IEEE International Conference on Space Optical Systems and Applications (ICSOS)*, (IEEE, 2015), pp. 1–6.
12. R. M. Calvo, P. Becker, D. Giggenbach, F. Moll, M. Schwarzer, M. Hinz, and Z. Sodnik, "Transmitter diversity verification on artemis geostationary satellite," *Proc. SPIE* **8971**, 897104 (2014).
13. D. M. Boroson and B. S. Robinson, "The lunar laser communication demonstration: Nasa's first step toward very high data rate support of science and exploration missions," *The lunar atmosphere and dust environment explorer mission (LADEE)* pp. 115–128 (2015).
14. D. Giggenbach, J. Poliak, R. Mata-Calvo, C. Fuchs, N. Perlot, R. Freund, and T. Richter, "Preliminary results of terabit-per-second long-range free-space optical transmission experiment thrust," *Proc. SPIE* **9647**, 96470H (2015).
15. R. M. Calvo, J. Poliak, J. Surof, A. Reeves, M. Richerzhagen, H. F. Kelemu, R. Barrios, C. Carrizo, R. Wolf, F. Rein, A. Dochhan, K. Saucke, and W. Luetke, "Optical technologies for very high throughput satellite communications," *Proc. SPIE* **10910**, 31 (2019).
16. N. Leonhard, R. Berlich, S. Minardi, A. Barth, S. Mauch, J. Mocchi, M. Goy, M. Appelfelder, E. Beckert, and C. Reinlein, "Real-time adaptive optics testbed to investigate point-ahead angle in pre-compensation of earth-to-geo optical communication," *Opt. Express* **24**(12), 13157–13172 (2016).
17. A. Brady, R. Berlich, N. Leonhard, T. Kopf, P. Böttner, R. Eberhardt, and C. Reinlein, "Experimental validation of phase-only pre-compensation over 494 m free-space propagation," *Opt. Lett.* **42**(14), 2679–2682 (2017).
18. A. Brady, C. Rössler, N. Leonhard, M. Gier, P. Böttner, R. Eberhardt, A. Tünnermann, and C. Reinlein, "Validation of pre-compensation under point-ahead-angle in a 1 km free-space propagation experiment," *Opt. Express* **27**(13), 17840–17850 (2019).
19. R. Saathof, R. den Breeje, W. Klop, N. Doelman, T. Moens, M. Gruber, T. Russchenberg, F. Pettazzi, J. Human, R. M. Calvo, J. Poliak, R. Barrios, M. Richerzhagen, and I. Ferrario, "Pre-correction adaptive optics performance for a 10 km laser link," *Proc. SPIE* **10910**, 109101H (2019).
20. N. Védrenne, J.-M. Conan, A. Bonnefois, C. Petit, M.-T. Velluet, and V. Michau, "Adaptive optics pre-compensation for geo feeder links: Towards an experimental demonstration," in *2017 IEEE International Conference on Space Optical Systems and Applications (ICSOS)*, (IEEE, 2017), pp. 77–81.
21. A. Montmerle Bonnefois, C. Petit, C. B. Lim, J.-F. Sauvage, S. Meimon, P. Perrault, F. Mendez, B. Fleury, J. Montri, J.-M. Conan, V. Michau, N. Védrenne, Z. Sodnik, and C. Voland, "Adaptive optics precompensation of a geo feeder link: the feedelio experiment," in *Applications of Lasers for Sensing and Free Space Communications*, (Optical Society of America, 2019), pp. LTh1B–3.
22. A. Montmerle Bonnefois, J. M. Conan, C. Petit, C. B. Lim, V. Michau, S. Meimon, P. Perrault, F. Mendez, B. Fleury, J. Montri, and N. Védrenne, "Adaptive optics pre-compensation for GEO feeder links: the FEDELIO experiment," in *International Conference on Space Optics – ICSO 2018*, (2019), p. 83.
23. D. L. Fried, "Optical resolution through a randomly inhomogeneous medium for very long and very short exposures," *J. Opt. Soc. Am.* **56**(10), 1372–1379 (1966).
24. R. J. Sasiela, *Electromagnetic wave propagation in turbulence: evaluation and application of Mellin transforms*, vol. 18 (Springer Science & Business Media, 2012).
25. J. W. Hardy, *Adaptive optics for astronomical telescopes*, vol. 16 (Oxford University, 1998).
26. R. K. Tyson and B. W. Frazier, *Principles of adaptive optics* (CRC, 2022).
27. N. Védrenne, V. Michau, C. Robert, and J.-M. Conan, "Cn2 profile measurement from shack-hartmann data," *Opt. Lett.* **32**(18), 2659–2661 (2007).
28. N. Védrenne, A. Montmerle Bonnefois, C. Robert, V. Michau, J. Montri, and B. Fleury, "Cn2 profile measurement from shack-hartmann data: experimental validation and exploitation," *Proc. SPIE* **7828**, 78280B (2010).
29. B. J. Klein and J. J. Degnan, "Optical antenna gain. I: Transmitting antennas," *Appl. Opt.* **13**(9), 2134–2141 (1974).
30. P. Lognoné, A. Montmerle Bonnefois, J.-M. Conan, L. Paillier, C. Petit, C. B. Lim, S. Meimon, J. Montri, J.-F. Sauvage, and N. Védrenne, "New results from the 2021 feedelio experiment—a focus on reciprocity," in *2022 IEEE International Conference on Space Optical Systems and Applications (ICSOS)*, (IEEE, 2022), pp. 261–266.
31. O. Farley, M. Townson, and J. Osborn, "Fast: Fourier domain adaptive optics simulation tool for bidirectional ground-space optical links through atmospheric turbulence," *Opt. Express* **30**(13), 23050–23064 (2022).
32. N. Védrenne, J.-M. Conan, C. Petit, and V. Michau, "Adaptive optics for high data rate satellite to ground laser link," *Proc. SPIE* **9739**, 97390E (2016).
33. L. Canuet, N. Védrenne, J.-M. Conan, C. Petit, G. Artaud, A. Rissons, and J. Lacan, "Statistical properties of single-mode fiber coupling of satellite-to-ground laser links partially corrected by adaptive optics," *J. Opt. Soc. Am. A* **35**(1), 148–162 (2018).
34. J.-M. Conan, A. Montmerle Bonnefois, N. Védrenne, C. Lim, C. Petit, V. Michau, M.-T. Velluet, J.-F. Sauvage, S. Meimon, C. Robert, J. Montri, F. Mendez, P. Perrault, G. Artaud, and B. Benammar, "Adaptive optics for geo-feeder links: from performance analysis via reciprocity based models to experimental demonstration," in

- COAT-2019-workshop (Communications and Observations through Atmospheric Turbulence: characterization and mitigation)*, (2019).
35. R. J. Noll, "Zernike polynomials and atmospheric turbulence," *J. Opt. Soc. Am.* **66**(3), 207–211 (1976).
 36. F. J. Rigaut, J.-P. Véran, and O. Lai, "Analytical model for shack-hartmann-based adaptive optics systems," in *Adaptive Optical System Technologies*, vol. 3353 (SPIE, 1998), pp. 1038–1048.
 37. B. Neichel, "Study of distant galaxies and tomographic adaptive optics for the elts," Tech. rep., Université de Paris VII (2008).
 38. J.-M. Conan, G. Rousset, and P.-Y. Madec, "Wave-front temporal spectra in high-resolution imaging through turbulence," *J. Opt. Soc. Am. A* **12**(7), 1559–1570 (1995).
 39. M. Demerle, P. Madec, and G. Rousset, "Servo-loop analysis for adaptive optics," *adaptive optics for astronomy* **423**, 73–88 (1994).
 40. G. C. Valley, "Isoplanatic degradation of tilt correction and short-term imaging systems," *Appl. Opt.* **19**(4), 574–577 (1980).
 41. F. Chassat, "Theoretical evaluation of the isoplanatic patch of an adaptive optics system working through the atmospheric turbulence," *J. Opt.* **20**(1), 13–23 (1989).
 42. J. Martin and S. M. Flatté, "Intensity images and statistics from numerical simulation of wave propagation in 3-d random media," *Appl. Opt.* **27**(11), 2111–2126 (1988).
 43. D. J. Link, "Comparison of the effects of near-field and distributed atmospheric turbulence on the performance of an adaptive optics system," in *Laser Beam Propagation and Control*, vol. 2120 (SPIE, 1994), pp. 87–94.
 44. E. Marchetti and C. Correia, "Object-oriented matlab adaptive optics toolbox," *Proc. SPIE* **9148**, 91486C (2014).
 45. E. Marchetti, "Soapy: an adaptive optics simulation written purely in python for rapid concept development," *Proc. SPIE* **9909**, 99097F (2016).
 46. C. B. Lim, A. Montmerle Bonnefois, C. Petit, J.-F. Sauvage, S. Meimon, P. Perrault, F. Mendez, B. Fleury, J. Montri, J.-M. Conan, V. Michau, and N. Védrenne, "Single-mode fiber coupling with adaptive optics for free-space optical communication under strong scintillation," in *2019 IEEE International Conference on Space Optical Systems and Applications (ICSOS)*, (IEEE, 2019), pp. 1–6.
 47. N. Védrenne, C. Petit, A. Montmerle Bonnefois, C. B. Lim, J.-M. Conan, L. Paillier, M.-T. Velluet, K. Caillault, F. Gustave, A. Durecu, V. Michau, F. Cassaing, S. Meimon, and J. Montri, "Performance analysis of an adaptive optics based optical feeder link ground station," *Proc. SPIE* **11852**, 1185219 (2021).
 48. C. Petit, A. Montmerle Bonnefois, J.-M. Conan, A. Durecu, F. Gustave, C. B. Lim, J. Montri, L. Paillier, P. Perrault, M.-T. Velluet, J.-B. Volatier, and N. Védrenne, "Feelings: the onera's optical ground station for geo feeder links demonstration," in *2022 IEEE International Conference on Space Optical Systems and Applications (ICSOS)*, (IEEE, 2022), pp. 255–260.
 49. J. L. Bufton, "Comparison of vertical profile turbulence structure with stellar observations," *Appl. Opt.* **12**(8), 1785–1793 (1973).
 50. O. Farley, J. Osborn, R. Wilson, T. Butterley, D. Laidlaw, M. Townson, T. Morris, M. Sarazin, F. Derie, M. Le Louarn, A. Chacón, X. Haubois, J. Navarrete, and J. Milli, "Representative atmospheric turbulence profiles for eso paranal," *Proc. SPIE* **10703**, 87 (2018).
 51. D. Sprung and E. Sucher, "Characterization of optical turbulence at the solar observatory at the mount teide, tenerife," *Proc. SPIE* **8890**, 321–329 (2013).
 52. H. Vázquez Ramió, J. Vernin, C. Muñoz-Tunón, M. Sarazin, A. M. Varela, H. Trinquet, J. M. Delgado, J. J. Fuensalida, M. Reyes, A. Benhida, Z. Benkhaldoun, D. García Lambas, Y. Hach, M. Lazrek, G. Lombardi, J. Navarrete, P. Recabarren, V. Renzi, M. Sabil, and R. Vrech, "European extremely large telescope site characterization. ii. high angular resolution parameters," *Publ. Astron. Soc. Pac.* **124**(918), 868–884 (2012).
 53. J. Osborn, M. J. Townson, O. J. Farley, A. Reeves, and R. M. Calvo, "Adaptive optics pre-compensated laser uplink to leo and geo," *Opt. Express* **29**(4), 6113–6132 (2021).